Numerical models for continental break-up: Implications for the South Atlantic

Anouk Beniest, Alexander Koptev, Evgenii Burov

Numerical models for continental break-up: implications for the South Atlantic

Beniest, A.[1, 2], Koptev, A.[1] Burov, E.[1†]

Email corresponding author: a.beniest@gmail.com

1. Sorbonne Universités, UPMC University Paris 06, CNRS, Institut des Sciences de la Terre de Paris (iSTeP), 4 Place Jussieu 75005 Paris, France
2. IFP Energies nouvelles, Geosciences, 1&4 Avenue du Bois-Préau 92852, Rueil-Malmaison, France

† Deceased 9 October 2015

Abstract

We propose a mechanism that explains in one unified framework the presence of continental break-up features such as failed rift arms and high-velocity and high-density bodies that occur along the South Atlantic rifted continental margins. We used 2D and 3D numerical models to investigate the impact of thermo-rheological structure of the continental lithosphere and initial plume position on continental rifting and breakup processes. 2D experiments show that break-up can be 1) "centred", mantle plume-induced and directly located above the centre of the mantle anomaly, 2) "shifted", mantle plume-induced and 50 to 250 km shifted from the initial plume location or 3) "distant", self-induced due to convection and/or slab-subduction/delamination and 300 to 800 km off-set from the original plume location. With a 3D, perfectly symmetrical and laterally homogenous setup, the location of continental break-up can be shifted hundreds of km's from the initial position of the mantle anomaly. We demonstrate that in case of shifted or distant continental break-up with respect to the original plume location, multiple features can be explained. Its deep-seated source can remain below the continent at one or both sides of the newly-formed ocean. This mantle material, glued underneath the margins at lower crustal levels, resembles the geometry and location of high velocity/high density bodies observed along the South Atlantic conjugate margins. Impingement of

vertically up-welled plume material on the base of the lithosphere results in pre-break-up topography variations that are located just above this initial anomaly impingement. This can be interpreted as aborted rift features that are also observed along the rifted margins. When extension continues after continental break-up, high strain rates can relocalize. This relocation has been so far attributed to rift jumps. Most importantly, this study shows that there is not one, single rift mode for plume-induced crustal break-up.

1. Introduction

Over the last decades a large variety of rift features have been recognised and explained with different methods and different concepts. These features include for example aborted rift structures, anomalous topography or anomalously high velocity/high density bodies located in the lower crust. Explanations for anomalous features often link one mechanism with one observed rift feature. For example, on plume impingement, a stratified lithospheric rheology (e.g. D'Acremont et al., 2003; Burov et al., 2007;) would result in topographic uplift, as has been modelled with thermo-mechanical modelling. Forward modelling shows that magmatic underplating can cause topographic variations (Hirsch et al., 2010). Anomalously high velocity/high density bodies have been observed on tomographic images below the continents, implying that in some regions magmatic processes dominate rifting (Cornwell et al., 2006). The latter is also suggested by gravity modelling that revealed the presence of anomalously high-density bodies in e.g. the South Atlantic domain, implying that volcanic activity played a key role in margin development (Blaich et al., 2011; Maystrenko et al., 2013).

Review papers combine all these studies on one specific topic. Examples are the role of the Moho in extensional settings (Cloetingh et al., 2013), the effect of volcanism in rifting and continental break-up (Franke, 2013) or the dynamic processes that control rifting (Ziegler and Cloetingh, 2004).

With this study we demonstrate how one break-up mechanism can explain a multitude of features. We use the South Atlantic break-up as our case study for plume-induced continental break-up. Since the South Atlantic developed diachronously and it is a very complex region requiring a 3D approach, we have not the intension to reproduce the South Atlantic evolution as such, including along-axis northward break-up

propagation to close to the plume (Franke, 2013), but rather to address general observations on continental break-up. Our fully coupled lithospheric-grade 2D and 3D models have an explicit elasto-visco-plastic rheology that accounts for realistic deformation of the lithosphere and a slip free surface that can calculate vertical motions. The 2D model has proven to be very useful to investigate plume-lithosphere interactions (e.g. d'Acremont et al., 2003; Burov et al., 2007). We take it one step further by developing one scenario to explain multiple anomalous features, such as high-velocity/high-density bodies and anomalous topographic variations with one single model. The 3D model is used to include the lateral component in a very simple, completely lateral homogeneous setting (Koptev et al., 2016).

2. Geological and geophysical setting

2.1. South Atlantic opening

Initial extension between Africa and South America was accommodated along a former fold-and-thrust belt (present-day location see Fig. 1), known as the Gondwana Fold Belt (GFB) or the Cape Fold Belt (CFB). This fold-and-thrust-belt was reactivated during the Early Mesozoic as a strike-slip system before the opening of the South Atlantic (Cobbold et al., 1992). During this reactivation it weakened the South American plate prior to the development of the Atlantic Mid-Oceanic Ridge, forming a first set of extensional basins (Autin et al., 2013), their axes oriented obliquely to the present-day orientation of the spreading centre (Fig. 1). Several extensional pulses caused the opening of the South Atlantic between 134 Ma and 113 Ma (e.g. Torsvik et al., 2009; Moulin et al., 2010). Voluminous volcanic activity, recognised on seismic reflection profiles as 'Seaward Dipping Reflectors' (SDR's) in the form of aerial flood basalts (extrusive) and/or underplating (intrusive) accompanied an episode of extension that created the South Segment (Fig. 1), starting between 134 Ma and 132 Ma (Moulin et al., 2010). Another pulse contributed to the formation of the Central Segment, starting around 112 Ma (Moulin et al., 2010) and is marked by massive salt deposits that have not been found along the margins of the South Segment (Fig. 1, Torsvik et al., 2009). Only minor volcanic activity has been recorded in this segment as the typical SDR's are mostly absent, except just north of the Rio Grande Rise (Franke, 2013). The opening of the South Atlantic and

formation of the Mid-Atlantic Ridge is considered to be due to a combination of passive far-field forces (Husson et al., 2012) and the presence of different hotspots (Torsvik et al., 2009). A major far-field stress component that enhanced the growth of the South Atlantic domain during the Mesozoic is the subducting and 'pulling' Nazca plate to the west of the South American continent, which also resulted in the faster west-ward migration of the South American plate with respect to the almost stationary African plate (e.g. Husson et al., 2012). The South-African super plume rises from the core-mantle boundary (CMB) to below the mantle transition zone (Hassan et al., 2015) which is reflected in present-day topography by a "superswell" at the margins of the south-west African continent (Nyblade and Robinson, 1994; Davaille et al., 2005). As shown by a.o. Lithgow-Bertelloni and Silver (1998), this excess of topography elevation is dynamically supported by upwelling flow of buoyant material through the mantle. From this large-scale, lower mantle low-velocity anomaly, the hotspots and their tracks (e.g. the Bouvet (Meteor), the Trinidad and St Helena Hotspots (Torsvik et al., 2006,2009)) and the only deep rooted Tristan plume (Fig. 1, Torsvik et al. (2009) and references therein) might develop over a long period of time (~200 Myr).

2.2. Lithosphere structure margins

The selected profile for our 2D model connects the offshore southwest Africa Orange Basin and its conjugate with the Colorado basin on the South American side (pink line, Fig. 1). The Tristan hotspot lies actually in the middle of the two transects (Fig. 1). The present-day crustal and lithosphere structure of these margins is constrained by combining published work on deep seismic refraction data, tomography, gravity and magnetic studies (Fig. 2).

On the African side of the transect (Fig. 2a) the lithosphere thickness ranges from 120 km below the oceanic crust to 200 km below the continent (Fishwick, 2010). With gravity modelling and seismic interpretation the Moho-depth has been estimated to be less than 10 km below the oceanic crust of the Orange basin and over 40 km below the continent (Maystrenko et al., 2013). Even though crustal movements have been observed in central Africa, the southern African plate is considered relatively stable with a strong rheology (Heine et al., 2013).

On the South American side the lithosphere-asthenosphere boundary (LAB) reaches depths of 160km below the stable continent in Eastern Brazil and 120 km in below the continent in Central Argentina (Heit et al., 2007). The Moho depth varies between 70 km below the plateau in the Andean orogeny to 25-35 km below the flat continent (Van Der Meijde et al., 2013). For the Colorado basin specifically, deep refraction seismic studies reveal a crustal thickness of the margins of 30 km (Franke et al., 2006).

We assume that before continental break-up, the lithosphere thickness of the South American plate was similar to that of the African plate. However, the South American plate underwent an earlier deformation phase prior to the formation of the South Atlantic domain (Autin et al., 2013). Extensional deformation does result in lithospheric thinning and weakening (Ziegler and Cloetingh, 2004). We, therefore, adopt a weaker strength compared to the African plate and a thickness of 180 km, which is the mean between the 200 km of the African lithosphere and the present-day 160 km South American lithosphere, to account for this earlier deformation phase.

2.3. High velocity/high density bodies and aborted rift structures

Along the South Atlantic conjugate margins high velocity/high density bodies have been described at lower crustal depths below the continent and the margin (Fig. 1) using seismic data and gravity modelling. Anomalous gravity and velocity bodies have been noted in the Central segment on the African side from Gabon (Dupré et al., 2007) to the Lower Congo (Contrucci et al., 2004) and the Kwanza Basin (Blaich et al., 2011) and on the South American side from the Sergipe-Alagoas Basin (Mohriak et al., 2000), to the Camamu-Atmada basin (Blaich et al., 2011) and the Santos basin (Blaich et al., 2011). In the South segment on the African side these bodies have been observed in the Walvis Basin (Blaich et al., 2011) and the Orange Basin (Dressel et al., 2015) and on the South American side in the Colorado basin, along the Uruguayan margin (Clerc et al., 2015) and in the deep Argentina Basin (Franke et al., 2006; Schnabel et al., 2008). These bodies differ from the seaward-dipping reflectors (SDR) as they are situated at the base of the lithosphere or at lower crustal levels and do not necessarily have a magmatic origin. They could be serpentinized mantle or mafic and ultramafic crustal rocks (Fig. 2, Blaich et al., 2011).

Graben structures or aborted rift structures onshore along the whole South American margin of the South Atlantic domain (Burke, 1976), are located near the anomalously high velocity/high density bodies. In the South Segment, graben structures and failed rift structures are less-abundant along the African margin, where they appear mainly along the south South-African margin and in the Central segment along the Gabon and Benin margins. On the South American side of the South Segment, the basins oriented perpendicular to the present-day ridge extend onshore as aborted rift features (Burke, 1976). Another failed rift feature is observed in the southwestern part of the Santos Basin, where the now aborted Abimael ridge is located parallel to the present-day Mid Oceanic Ridge (Heine et al., 2013).

3. Model setup

The 2D thermo-mechanical numerical code FLAMAR, based on the FLAC-Para(o)voz algorithm (Cundall, 1989; Poliakov et al., 1993) has been used to investigate the effect of plume location on continental break-up using the South-Atlantic as an example of a fully developed rift-to-spreading system. We built our case on the continuation of earlier parametric studies on the rheology of the lithosphere and plume-continental lithosphere interactions (D'Acremont et al., 2003; Burov et al., 2007). Where needed, we adjust the parameters according to the geological and geophysical evidence described above. A symmetric simulation that is not area-specific are carried out with the 3D viscous-plastic numerical code 3DELVIS (Gerya and Yuen, 2007). All mechanical and thermo-rheological parameters are listed in Table 1. We have performed a series of 36 experiments. Controlling parameters and principal results are summarized in Table 2.

3.1. 2D numerical model

The FLAMAR code has been updated and modified over the last 20 years (Burov and Diament, 1995; Burov and Poliakov, 2001; Le Pourhiet et al., 2004; Yamato et al., 2008). For the sake of coherency with previously published papers we only describe the main features and essentials of the model used for this study. Detailed descriptions of the code can be found in studies that have tested the code for many different geological cases (D'Acremont et al., 2003; Le Pourhiet et al., 2004; Yamato et al., 2008). FLAMAR is a fully explicit, finite

element/finite difference code based on a Cartesian coordinate frame. It has a 2D strain formulation with a Lagrangian mesh that consists of quadrilateral elements consisting of two couples of triangular sub-elements containing tri-linear shape functions. It uses a large-strain, time-marching scheme. The code solves for full Newtonian equations of motions in a continuum mechanics approximation (3.1)

$$< \rho \ddot{\boldsymbol{u}} > -\nabla\sigma - \rho \boldsymbol{g} = 0 \quad (3.1)$$

where ρ, $\ddot{\boldsymbol{u}}$, σ and **g** stands for density, acceleration of the object, stress and acceleration due to body forces or gravity, respectively.

It is coupled with constitutive laws (3.2) to quantify viscous, elastic and plastic characteristics by the heat transfer equation (3.3), where the heat advection term ($\dot{\boldsymbol{u}}\nabla T$) is included in the Lagrangian derivative (DT/Dt). Erosion and sedimentation is accounted for using a linear diffusion equation assuming conversation of mass (3.4).

$$\frac{\mathrm{D}\sigma}{\mathrm{D}t} = F(\sigma, \boldsymbol{u}, \dot{\boldsymbol{u}}, \boldsymbol{\nabla}\dot{\boldsymbol{u}}, T) \quad (3.2)$$

$$\rho C_p DT/Dt - k\nabla^2 T - \sum_i^n H_i = 0; \qquad \rho = f(P, T) \quad (3.3)$$

$$\frac{dh}{dt} = a\nabla^2 h \quad (3.4)$$

In this case, *t* stands for time, **u** is the displacement vector, and *T* is temperature. The heat transfer equation relies on C_p for the specific heat, *k* for thermal conductivity respectively and *H* for the internal heat production, including radiogenic heat and frictional heat dissipation. *P* stands for pressure that become negative for compression. The linear diffusion equation uses a constant *a* and the height or thickness of the sediments *h*.

The code is capable of calculating realistic visco-elasto-plastic rheologies explicitly. Pressure-dependent deformation is maintained through the Mohr-Coulomb criteria for the plastic regime and the non-linear viscous flow law at depth. The free surface upper boundary condition calculates high-resolution topographic changes due to deformation of the lithosphere.

3.1.1. Model geometries

The model box is 2000 km wide and 400 km deep. The grid size is 400 x 80 elements, resulting in a resolution of 5 km x 5 km per element. We have tested three different lithospheric setups with diverse complexities (see 3.1.2, Fig. 3) and three different locations of a 1700^{o}C thermal and compositional mantle anomaly at 400 km depth (D'Acremont et al., 2003). The initial locations vary laterally at the base of the model with the center of the anomaly positioned 1) at the centre of the model (i.e. plume location at 1000 km, see Table 2), 2) at 200 km to the right of the model box's centre (i.e. plume location at 1200 km) and 3) at 200 km to the left of the model box's centre (i.e. plume location at 800 km). Each location is tested in a separate calculation. Following previous studies the base of the anomaly lies at 400 km depth as the deeper mantle phase does not have a large impact on the crustal evolution (D'Acremont et al., 2003; Ribe and Christensen, 1994). The anomaly has a simplified, symmetric, spherical shape since at depth viscous bodies take a spherical shape and this follows the line of 2D and 3D numerical modelling experiments on plume-lithosphere interaction (a.o. D'Acremont et al., 2003; Burov and Gerya, 2014; Koptev et al., 2016). In most of the experiments, it has a diameter of 230 km. The effects of a mantle anomaly with a diameter of 100 km were tested in a limited number of models. The composition of the mantle anomaly is olivine with a density of 3250 kg/m^3 (except for several models where it is 3310 kg/m^3) which has been determined to be an intermediate plume in previous studies (Turcotte and Schubert, 2002; D'Acremont et al., 2003). No background density tests have been performed as the background density used for background calculations is the same for the plume as well as the surrounding mantle. The thermal contrast between the plume and the mantle varies as thermal exchanges happen between the plume and the mantle, decreasing the temperature of the plume. The mantle also cools as the plume rises to shallower depths.

3.1.2. Density and rheological structure

The 2D model consists of four horizontal rheological layers. For Setup 1 (Fig. 3a and Fig. 3b), a laterally homogeneous 40 km thick two-layered crust and a 160 km thick lithospheric mantle have been applied. We test the model's sensitivity for two different rheological properties of the crust. We use a "weaker" rheological strength envelope (Setup 1a; Fig. 3a), composed of 1) a wet quartz upper crust with a density of

208 2500 kg/m^3 and 2) a diabase lower crust with a density of 2750 kg/m^3. Our second rheological strength
209 envelope has the characteristics of a "strong", cratonic crust that consists of: 1) a dry quartz upper crust with
210 a density of 2600 kg/m^3 and 2) a strong diabase lower crust with a density of 2850 kg/m^3. The rheological
211 differences of the two strength envelopes represent a "weaker" crust that has been subject to an earlier
212 deformation phase, before the opening of the South Atlantic, which is the case for the South American side
213 (Autin et al., 2013), and a "stronger" crust of cratonic nature that represents the stable southern African
214 continent(after Burov and Diament, 1995). Dry olivine flow law has been assumed for both lithospheric and
215 sub-lithospheric mantle in all our experiments. The initial density of the mantle decreases from 3330 kg/m^3
216 to 3310 kg/m^3 at the lithosphere-asthenosphere boundary. Specific values of the rheological parameters used
217 are given in Table 1.
218 For Setups 2 and 3 we apply a laterally non-homogeneous crustal rheology: a "weak" crustal rheology for
219 the left half of the model and a "strong" crustal rheology for the right one (Fig. 3c-f). The crustal and
220 lithospheric thicknesses are laterally homogeneous in Setup 2a: 20 km for upper crust, 20 km for lower crust
221 and 160 km for lithospheric mantle (Fig. 3c). Setups 2b and 3 are characterized by laterally varying
222 lithospheric layers, based on the lithospheric scale structure described in section 2.2: the "weaker" left half
223 has a 15 km-thick upper crust, 15 km-thick lower crust and a 150 km-thick lithospheric mantle, whereas the
224 "stronger" right half has a 20 km-thick upper crust, a 20-km think lower crust and a 160 km-thick
225 lithospheric mantle (Fig. 3c-f). Three different contacts between the rheological strengths are tested. Setup
226 2b has a straight vertical contact. For Setup 3 we have adopted a geometry resembling the old suture zone
227 that is reactivated during the first extensional phase. The suture is dipping either 40 degrees towards the
228 'strong', African rheology (Setup 3a) or towards the 'weak' South American rheology (Setup 3b).
229 By the setups described above we have tested the following parameters: initial position of the plume, density
230 of the mantle plume (limited to Setup 3a) and different half-rate velocity boundary conditions (see Table 1).
231
232 *3.1.3. Mechanical and thermo-rheological boundary conditions*

We simulate tectonic forcing by applying a constant, time independent, extension rate along the vertical side of the box of 25 mm/yr. An equal half-rate velocity is applied on both sides of the box (12.5 mm/yr) to one set of models and 5 mm/yr on the right side and 20 mm/yr on the left side is applied to a second set of models (Table 1). The half-rate velocities are adopted from (Müller et al., 2008). The bottom of the box is defined by hydrostatic pressure with free slip in all directions. The upper side of the box is a free surface boundary, implying a free stress and a free slip condition in all direction, allowing the lithosphere to develop freely. A moderate erosion by diffusion is applied (a = 500 m^2/yr).

The upper and bottom thermal boundary condition is a fixed temperature 10 ^oC and 1400 ^oC respectively to represent a 'cold' geotherm. An old lithosphere of 500 Ma (Burov and Diament, 1995) has been assumed for the tectonic age used to represent the super-continent Pangea before break-up. The geotherm used for the models reaches 500 ^oC at Moho depth, 1330 ^oC at the lithosphere-asthenosphere boundary (LAB) after which it becomes adiabatic until it reaches 1400 ^oC at the base of the model at 400 km (Ribe and Christensen, 1994).

3.2. 3D numerical model

A 3D model has been performed with the thermo-mechanical viscous-plastic 3DELVIS code (Gerya, 2010; Gerya and Yuen, 2007) that combines the finite difference method with a marker-in-cell technique. The 3D model box has the horizontal dimensions 1500 × 1500 × 635 km and consists of 297 × 297 × 133 nodes offering spatial resolution of ca. 5 × 5 × 5 km per grid cell. Not area-specific initial setup consists of a stratified three-layer (upper/lower crust and lithospheric mantle) continental lithosphere underlain by an asthenosphere. The total thickness of the two-layer crust is 36 km; the depth of lithosphere-asthenosphere boundary is 150 km. The mantle plume has been seeded at the base of the modelled domain by a spherical thermal anomaly of 370 ^oC with a radius of 200 km. The initial geotherm is piece-wise linear with fixed temperatures at the surface (0°C), at the Moho (700°C), at the base of the lithosphere (1300°C), and at the bottom of the model box (1630°C). Weak tectonic forcing has been simulated by applying a constant ultra-slow divergent horizontal velocity of 3 mm/year along the sides of the model. More detailed information on

the 3D model setup and rheological and material properties used in our 3D experiments can be found in Burov and Gerya (2014) and Koptev et al. (2015, 2016).

4. Model results

4.1. 2D model results

Three types of model scenarios result from our set of experiments. "Centred" break-up, when the mantle anomaly moves vertically upwards and break-up happens directly above the original location of the centre of the mantle anomaly. "Shifted" break-up, when the mantle anomaly first migrates vertically and, once it reaches the base of the lithosphere, migrates laterally until break-up occurs with a 50 to 250 km offset with respect to the initial anomaly position. "Distant" break-up, when a mantle anomaly rises to the base of the lithosphere and remains there, while the location of break-up takes place more than 300 km away from the initial site of the anomaly.

Experiment 6, characterized by a "strong" homogenous lithosphere, is an example of "centred" break-up (Fig. 4a). The mantle anomaly reaches the base of the lithosphere rapidly within 2 Myr, after which it penetrates into the lithosphere. The rising flow of plume material is strong enough to break apart the overlying lithospheric mantle and crust between 7 and 8 Myr. The surface reacts by uplift, then subsidence and alternating positive and negative vertical movements of the margins and the rift centre. Although the initial position of break-up centre is situated directly above mantle plume, the continuous extensional evolution, including strain relocation and changing temperature distribution, suggest a post-rift lateral shift of the spreading axis. Note that after continental break-up mantle plume material reaches the surface where it contributes to the formation of new oceanic lithosphere.

The "shifted" mode of continental break-up is illustrated by Experiment 12 where the mantle plume anomaly has been seeded below a stronger lithosphere composing the right half of the model domain (Fig. 4b). As in the case of Experiment 6, the onset of rifting starts with a rapid rise of the anomaly, impinging the lithosphere not later than 2 Myr. Surface topography associated with localized crustal strain is formed around 3-4 Myr with small offset (<50 km) from the point directly above mantle plume impingement.

Further upslope migration plume material leads to continental break-up between 7 and 10 Myr. A principal difference from the "centred" experiment 6 is the lateral shift (50 to 250 km) of the newly formed spreading axis with respect to the initial position of the mantle plume. Lateral migration of the plume head to this break-up axis leads to an asymmetrical distribution of the plume material: some of the material reaches the surface at the spreading centre, another part remains glued beneath the highly thinned lithosphere at depths between 200 and 10 km. Similar to Experiment 6, the final stage of the "shifted" system development is the strain relocation corresponding to 200 km-wide jump of the spreading axis.

Finally, experiment 16 illustrates the "distant" break-up mode that starts with a rapid uplift of the mantle plume to the bottom of the lithosphere, an observation typical for all performed models. This expectedly results in associated topography variations (Fig. 4c). In contrast with the two previously discussed break-up modes (experiments 6 and 12), mantle plume material remains glued beneath the base of the lithosphere without localized ascent towards the formed break-up centre. Lithosphere thinning that will result in break-up occurs at large distance (more than 500 km) from the plume impingement. This appears to be related to secondary mantle convection associated with plume-induced subduction of the lithospheric mantle that has developed upon plume upwelling to the lithosphere-asthenosphere boundary on both sides of the plume head. It is noteworthy that initial topographic changes created by the impingement of the plume remain visible throughout the model evolution. Given the lack of near-surface plume material, this "distant" mode cannot be considered as break-up directly induced by the impact of the mantle plume. Nevertheless, it might reflect the implicit influence of the upwelled plume on "distant" break-up processes via plume-induced subduction and mantle convection.

"Centred" break-up preferably takes place using initial Setup 1, where the crust and lithospheric mantle are laterally homogeneous and no inherited structures are given (Fig. 4a, Table 1), but other setups can also evolve according to this mode (Fig. 5a-c). Break-up occurs between 6 and 10 Myr, directly above the initial location of the mantle anomaly. Mantle material reaches the surface at the point of impingement that evolves into the break-up axis. Almost all plume material is involved in formation of new oceanic lithosphere. As a result, after continuous (more than 10 Myr) calculations, only little material remains below the thinned

continental lithosphere. Note that, even though central located plumes are expected to develop to a symmetric or "central" mode, a central located plume evolves the least likely into "central" type of break-up (table 1). "Shifted" break-up is favoured by Setup 2a where the thickness of the lithospheric layers is laterally homogeneous but crustal rheology differs (Fig. 5d-f). The mantle anomaly rises and break-up also occurs between 6 and 10 Myr, but in this case it is shifted from the initial point of impingement. Most mantle material remains below the lithosphere, but through migration along the bottom of the lithosphere some material still reaches the surface. This mode of break-up only occurs when the lithosphere properties (rheology and/or thickness) varies laterally, but it does not completely control "shifted" break-up, because not all laterally varying rheology experiments result in "shifted" break-up. Plume location is also not a controlling factor for the model to result in "shifted" break-up as all three plume locations can result in "shifted" break-up. The "distant" break-up experiments have a preference for Setup 2 and 3, where both the lithospheric layers' thickness and the crustal rheology are laterally different (Fig. 5g-i). Crustal break-up happens slightly later compared to the "centred" and "shifted" experiments: between 9 and 12 Myr. Mantle anomaly material does not reach the surface, but remains completely glued to the bottom of the lithosphere. Most of the continental break-up modelled with the "distant" experiments occurs in the lithospheric segment that is characterized by a strong crust.

Almost half (12 out of 25) of the equal half-rate velocities boundary condition results in "centred" break-up. More than half (6 out of 11) of the unequal half-rate velocity boundary conditions result in "distant" break-up mode. The different velocity parameters do have a preference for a certain break-up style, but it is not a controlling factor.

The models that resulted in "shifted" break-up have a mantle anomaly that rises to the base of the lithosphere and upon arrival, migrates, in most cases, towards the weaker lithosphere to break through this less strong segment. This is in contrast with the "distant" model results that develop crustal break-up in the stronger lithosphere (11 out of 11 models) when the plume remains glued below the weaker lithosphere and does not break through. In case of "distant" break-up mode, the rheology is very important and strongly controls this mode of break-up.

337

338 *4.2. 3D model results*

339 Similarly to the 2D experiments, the 3D model shows a quick (<2 Myr) upwelling of the plume material up
340 to lithosphere-asthenosphere boundary (Fig. 6a). After this, the plume head starts to spread laterally within
341 lower part of lithospheric mantle (Fig. 6b-d). When the mantle plume impinges on the base of lithosphere,
342 almost all plume material is partially melted (Fig. 6a). Following spreading and cooling expectedly leads to
343 gradual solidification of the plume (Fig. 6b-c), which has been completed at 50 Myr (Fig. 6d).
344 The interplay between far-field forces and active mantle upwelling results in a "classical" single rift that
345 crosses the entire model domain in the direction perpendicular to external extension (Fig. 6a). Continuous
346 evolution shows the formation of a wide rift valley where localized brittle deformation is concentrated along
347 the boundary fault (Fig. 6b-c). This rift basin opens rapidly (Fig. 6b) reaching a width of 600 km in less than
348 35 Myr while passive extension applied at the boundaries would result in only 200 km width (Fig. 6c). This
349 highlights the important role of plume-related buoyancy forces in the context of studied "active-passive"
350 rifting.
351 The next stage of the system evolution (65 Myr) is a quick switch of deformation localization from rift-
352 bounding faults to narrow zones inside the rift valley (Fig. 6e). This change in rifting style is caused by
353 initiation of localized upwelling of plume material along stretched zone(s) highlighted at the surface by
354 localized high strain rates (Fig. 6e). Further localized plume ascent associated with decompression melting
355 of plume material increases the rate of lithospheric thinning leading to continental break-up along a
356 spreading axis that has shifted laterally outwards from the centre of the plume head (Fig. 6f). This
357 asymmetrical position of the spreading zone arises spontaneously within initially symmetrical and laterally
358 homogenous lithosphere and is likely controlled by melting and cooling processes into head of mantle
359 plume.
360 Thus, a lateral shift of plume-induced break-up centres with respect to initial plume impingement revealed
361 in certain 2D experiments (see for example Experiment 6, Fig. 4a) appears to be an intrinsic characteristic
362 of self-induced plume-related processes that do not necessary requires fast (>1 cm/y) external extension nor

any lateral lithospheric heterogeneity (see also Experiment 2 for a 2D example of "distant" break-up in the context of laterally homogenous lithosphere).

5. Discussions

5.1. General aspects

The results of our models are important in the context of ongoing discussion on plume-induced continental break-up. We show that continental break-up can be initiated by just one single mantle plume under different initial and boundary conditions. In most of our 2D models (32 out of 36) continental break-up takes place as a result of the direct ("centred" or "shifted" modes) or indirect ("distant" mode) impact of the mantle plume (Fig. 8). Four remaining models do not result in break-up. On one hand, the models that develop according to "centred" (Fig. 8b) or "shifted" (Fig. 8c) modes are directly induced by the plume anomaly which results in penetration of plume material up to the surface. On the other hand, the "distant" mode is characterized by secondary mantle convection associated with plume-induced *subduction* and/or *convection*. In this case, the mantle plume is not involved directly in break-up processes and remains glued at the base of adjacent unbroken lithosphere (Fig. 8d).

In a very early phase, strain rate localizes and topographic variations develop directly above the initial plume impingement location (Fig. 8a). They remain visible only in the "shifted" and "distant" models and can be interpreted as aborted rifts. It was commonly accepted and almost self-evident that in the case of plume-induced continental break-up, its axis should be situated directly above the initial plume impingement position (D'Acremont et al., 2003). However, observations such as failed rifts and deep-seated mantle sources beneath a strong continent that are significantly remote from the mid-oceanic ridge, actually imply that continental rifting and break-up are not a purely symmetric and "plume-centred" processes. Our modelling demonstrates that symmetric development of mantle material ascent and subsequent continental break-up are not a definite outcome. More than half of our models (19 out of 32) result in "shifted" and "distant" break-up modes, suggesting that these modes should also be expected in a wide range of initial and boundary conditions. Even so, our perfectly symmetric and lateral homogeneous 3D model shows that

in a purely symmetric setting, with no lithospheric rheological heterogeneities, continental break-up shifted from the original centre of the mantle anomaly is possible. We argue here that "centred" symmetric continental break-up developed directly above mantle plume is only one particular case of possible evolutions of plume-induced break-up systems.

5.2. The case of the South Atlantic

The South Atlantic is considered to be a good example of plume-induced continental break-up (e.g. Torsvik et al., 2009). Some of the observations such as failed rifts (Heine et al., 2013) and high velocity bodies (e.g. Blaich et al., 2011) cannot be explained with conventional models, usually assuming a "centred"-like break-up style (e.g. Burov et al., 2007; D'Acremont et al., 2003). Yet, our experiments showing "shifted" break-up mode (Fig. 7; Fig. 8c) can be used to explain these features. In these models, initial crustal deformation associated with mantle plume impingement (Fig.7a-b; Fig.8a) are formed within the first 5 Myr. Significant topography variations developed during this initial stage of rift evolution (i.e. before break-up) can be interpreted as very early failed rift features (e.g. the failed Abimael rift in the southwest of the Santos Basin). The topographic plateaus that remain elevated long after break-up have also been observed with dynamic topography studies (Nyblade and Robinson, 1994). Next, localized strain becomes concentrated close to the boundary between strong and weak lithosphere that is laterally offset (~400 km) from the area of initial plume impingement (Fig.7c). Transition from wide rift stage to lithospheric break-up is marked by narrowing a broad rift region (over 1000 km width) down to narrow rift valley (Fig. 7c-d) with the width of 10's of kilometers between the two rift-shoulders. Associated lithospheric thinning leads to a separation of the two plates along a spreading centre corresponding to South Atlantic ridge (Fig.7e; Fig.8c). Part of strong crust that remains attached to the weaker lithosphere segment, could correspond to the Brazilian craton that was once bordering the African continent (Heine et al., 2013).

Simultaneously with thinning of the lithosphere below the future break-up centre, the plume material migrates along the base of the lithosphere and rises towards the deformed crust where it breaks through. This migration can go as far as 300 km from the plume impingement point and only ceases when the material

that is still at the base of the lithosphere (at depths between 200 km and 10 km) reaches thermal equilibrium (in this case after 22 Myr). This confirms the hypothesis that one mantle anomaly (or plume) can flow laterally over significant distances below a slow-moving continent, after being risen to the base of the lithosphere (e.g. Sleep, 2006). When thermal equilibrium is reached, the mantle material glued to the base of the lithosphere at shallower depths corresponds geometrically and location-wise to high-velocity/high-density bodies observed on seismic data below the thinned continental lithosphere and the transition zone of the South Atlantic domain (Clerc et al., 2015). During migration, products of partial melting of the mantle material can move vertically to (shallow) lower crustal levels. They might resemble high density bodies observed at lower crustal levels inside continental crust with similar geometries observed with gravity modelling (Blaich et al., 2011). These processes cannot be reproduced by our 2D modelling, because no melt production and extraction have been simulated.

Note that our 2D study has not the intention to capture such 3D features like along-axis northward propagation of the break-up axis (Franke, 2013) up to the centre of the surface manifestation of Tristan plume activity – the Paraná-Etendeka continental flood basalts province.

After continental break-up, the mantle plume anomaly continues to play an important role in the spreading evolution of the system. Strain rate relocation takes place around 18 Myr, when the spreading axis shifts another 200 km towards the left from the original position of the break-up centre (Fig. 7f). This phenomenon could correspond to a rift-jump that have also been both observed and modelled (Brune et al., 2014) in the South Atlantic domain.

The question we raised about the initial position of the mantle plume anomaly responsible for continental break-up in the South Atlantic remains open. On figure 8e, we show a reconstructed configuration of the slow velocity anomaly (corresponding to the South African Super Plume) at the CMB based on present-day seismic tomography model (after Davaille et al., 2005). The orange dots refer to the three possible principal locations of initial thermal anomaly at the upper/lower mantle boundary corresponding to the Tristan plume. The central point refers to the most evident “centered” scenario (Fig. 8b) when the deep-seated thermal anomaly in the upper mantle is supposed to be located directly below its surface manifestation and hints to

voluminous Paranà-Etendeka continental flood basalts province (Fig. 8e, e.g. Torsvik et al., 2009; Heine et al., 2013). This scenario, however, is not consistent with the commonly considered concept that plumes emerge from the edges of the large low-velocity anomalies at the CMB that has been confirmed by both numerical modelling (Hassan et al., 2015) and by empirically established correlation between downward projected plume-associated large igneous provinces and the margins of the large low shear velocity province beneath Africa (Torsvik et al., 2006). Moreover, with this 'centred' scenario we cannot explain additional features such as failed rift arms and anomalous bodies at lower crustal levels. The 'distant' break-up mode (Fig. 8d), where the initial plume centre is located below the South American section and remains there after "plume-independent" continental break-up, does not fit well with geological observations of the voluminous Paranà-Etendeka continental flood basalts that are supposed to be related with direct influence of the Tristan hot spot (Torsvik et al., 2009). Finally, initial plume position slightly moved to African side (right dot on Fig. 8e) refers to "shifted" scenario that seems to be preferable (Fig.8c). The time length of the modelled rift phase (10 Myr +/- 3 Myr) is much shorter than has been inferred from geological and geophysical observations (160 Ma to 134 Ma, (Franke, 2013)) in the South Segment of the South Atlantic. Despite this, with the eastward offset initial position of the mantle plume with respect to a heterogeneous thermo-rheological lithospheric structure we are able to explain not only plume induced flood basalts but also a set of anomalous features such as failed rift systems, and deep crustal bodies.

6. Conclusion

Different lithospheric strengths comparable to the South American and African continental crust, inherited structures, boundary velocity conditions corresponding to average spreading rates, and initial location of a thermal mantle anomaly (i.e. plume) have been tested to investigate the dynamics of plume induced continental break-up. A set of 36 models shows that with only one anomaly three very different scenarios for continental break-up can be realized depending on the rheological structure, anomaly location and inherited structures. Continental break-up does not necessarily occur above the centre of the initial location

of a mantle anomaly. As mentioned above, our models show three types of break-up 1) "centred" break-up, 2) "shifted" break-up and 3) "distant" break-up.

"Centred" and "shifted" break-up types of models refer to plume-induced type of break-up. For the first mode, mantle material rises vertically towards the bottom of the lithosphere after which it breaks through the crust and reaches the surface directly above the initial plume position. The "shifted" type of break-up shows continental break-up that is 50 to 200 km shifted from the initial location of the mantle anomaly. In this case, the mantle plume rises and impinges the lithosphere, after that it migrates laterally and cuts through the lithosphere reaching the surface at a break-up point considerably shifted from the area of initial, pre-break-up impingement. Some material remains glued underneath the lithosphere at depths between 200 and 10 km. These deep-seated bodies, at depths of 200 km, are not situated directly below the break-up centre, but are spread over a large area below the continental margins. The shallower bodies geometrically resemble high density/high velocity bodies detected by seismic profiling and gravity modelling along the margins of the South Atlantic domain and at lower crustal levels.

The "distant" break-up mode refers to continental rupture that is indirectly induced by the presence of the mantle plume ponding at the bottom of the weaker continental lithosphere, when "plume-independent" break-up of adjacent stronger lithosphere appears to be considerably (from 250 and 800 km) displaced from the location of plume-lithosphere interaction. In this case, laterally widely spread plume material remains glued below unbroken segments of the lithosphere.

Topographic changes that occur very early during initial rifting stage remain visible for a long period and can possibly be interpreted as failed rift systems (in the cases of "shifted" and "distance" modes). Strain relocation after continuous post-break-up extension could be interpreted as rift jumps. A simple 3D model has been built to illustrate that even in a fully symmetric setup, rift-to-break-up processes are not by default symmetric and can very well evolve asymmetrically.

There is no controlling parameter for one of the three types of rifting, with a combination of parameters determining the outcome, but the location of the mantle anomaly with respect to the rheology is the most

essential. The most important result of this study is that there is not one single rift mode for plume-induced crustal break-up.

7. Acknowledgment

This study is co-funded by the Advanced ERC Grant 290864 RHEOLITH to A. Koptev and E.Burov. 3D numerical simulations were performed on the ERC-funded SGI Ulysse cluster of ISTEP. We thank William Sassi (IFPEn), Xavier Guichet (IFPEn) and Sylvie Leroy (UPMC) for fruitful discussions in the early phases of the project. We would also like to thank Sierd Cloetingh (Utrecht University) for constructive and thorough reading of the manuscript. The two anonymous reviewers are also thanked for their helpful remarks and critical points of view.

8. References

Autin, J., Scheck-Wenderoth, M., Loegering, M.J., Anka, Z., Vallejo, E., Rodriguez, J.F., Dominguez, F., Marchal, D., Reichert, C., di Primio, R., Götze, H.-J., 2013. Colorado Basin 3D structure and evolution, Argentine passive margin. Tectonophysics 604, 264–279. doi:10.1016/j.tecto.2013.05.019

Blaich, O.A., Faleide, J.I., Tsikalas, F., 2011. Crustal breakup and continent-ocean transition at South Atlantic conjugate margins. J. Geophys. Res. 116, 1–38. doi:10.1029/2010JB007686

Brune, S., Heine, C., Pérez-Gussinyé, M., Sobolev, S. V, 2014. Rift migration explains continental margin asymmetry and crustal hyper-extension. Nat. Commun. 5, 1–9. doi:10.1038/ncomms5014

Burke, K., 1976. Development of graben associated with the initial ruptures of the Atlantic Ocean. Tectonophysics 36, 93–112.

Burov, E., Gerya, T., 2014. Asymmetric three-dimensional topography over mantle plumes. Nature 513, 85–89. doi:10.1038/nature13703

Burov, E., Guillou-Frottier, L., D'Acremont, E., Le Pourhiet, L., Cloetingh, S., 2007. Plume head-lithosphere interactions near intra-continental plate boundaries. Tectonophysics 434, 15–38.

516 doi:10.1016/j.tecto.2007.01.002
517 Burov, E., Poliakov, A., 2001. Erosion and rheology controls on synrift and postrift evolution: Verifying
518 old and new ideas using a fully coupled numerical model. J. Geophys. Res. 106, 16461–16481.
519 doi:10.1029/2001JB000433
520 Burov, E.B., Diament, M., 1995. The effective elastic thickness (Te) of continental lithosphere: What does
521 it really mean? J. Geophys. Res. 100, 3905–3927. doi:10.1029/94JB02770
522 Clerc, C., Jolivet, L., Ringenbach, J.C., 2015. Ductile extensional shear zones in the lower crust of a
523 passive margin. Earth Planet. Sci. Lett. 431, 1–7. doi:10.1016/j.epsl.2015.08.038
524 Cloetingh, S., Burov, E., Matenco, L., Beekman, F., Roure, F., Ziegler, P.A., 2013. The Moho in
525 extensional tectonic settings: Insights from thermo-mechanical models. Tectonophysics 609, 558–
526 604. doi:10.1016/j.tecto.2013.06.010
527 Cobbold, P.R., Gapais, D., Rossello, E.A., Milani, E.J., Szatmari, P., 1992. Permo-Triassic
528 intracontinental deformation in SW Gondwana. Invers. Tectonics Cape Fold Belt, Karoo Cretac.
529 Basins South. Africa 23–26.
530 Contrucci, I., Matias, L., Moulin, M., Géli, L., Klingelhofer, F., Nouzé, H., Aslanian, D., Olivet, J.L.,
531 Réhault, J.P., Sibuet, J.C., 2004. Deep structure of the West African continental margin (Congo,
532 Zaïre, Angola), between 5°S and 8°S, from reflection/refraction seismics and gravity data. Geophys.
533 J. Int. 158, 529–553. doi:10.1111/j.1365-246X.2004.02303.x
534 Cornwell, D.G., Mackenzie, G.D., England, R.W., Maguire, P.K.H., Asfaw, L.M., Oluma, B., 2006.
535 Northern Main Ethiopian Rift crustal structure from new high-precision gravity data. Geol. Soc.
536 London, Spec. Publ. 259, 307–321. doi:10.1144/GSL.SP.2006.259.01.23
537 Cundall, P.A., 1989. Numerical experiments on localization in frictional materials. Ingenieur-Archiv 59,
538 148–159.
539 D'Acremont, E., Leroy, S., Burov, E.B., 2003. Numerical modelling of a mantle plume: the plume head–
540 lithosphere interaction in the formation of an oceanic large igneous province. Earth Planet. Sci. Lett.
541 206, 379–396. doi:10.1016/S0012-821X(02)01058-0

Davaille, A., Stutzmann, E., Silveira, G., Besse, J., Courtillot, V., 2005. Convective patterns under the Indo-Atlantic « box ». Earth Planet. Sci. Lett. 239, 233–252. doi:10.1016/j.epsl.2005.07.024

Dressel, I., Scheck-Wenderoth, M., Cacace, M., Lewerenz, B., Götze, H.-J., Reichert, C., 2015. Reconstruction of the southwestern African continental margin by backward modelling. Mar. Pet. Geol. 67, 544–555. doi:10.1016/j.marpetgeo.2015.06.006

Dupré, S., Bertotti, G., Cloetingh, S., 2007. Tectonic history along the South Gabon Basin: anomalous early post-rift subsidence. Mar. Pet. Geol. 24, 151–172. doi:10.1016/j.marpetgeo.2006.11.003

Fishwick, S., 2010. Surface wave tomography: Imaging of the lithosphere – asthenosphere boundary beneath central and southern Africa? Lithos 120, 63–73. doi:10.1016/j.lithos.2010.05.011

Franke, D., 2013. Rifting, lithosphere breakup and volcanism : Comparison of magma-poor and volcanic rifted margins. Mar. Pet. Geol. 43, 63–87. doi:10.1016/j.marpetgeo.2012.11.003

Franke, D., Neben, S., Schreckenberger, B., Schulze, A., Stiller, M., Krawczyk, C.M., 2006. Crustal structure across the Colorado Basin, offshore Argentina. Geophys. J. Int. 165, 850–864. doi:10.1111/j.1365-246X.2006.02907.x

Gerya, T., 2010. Dynamical instability produces transform faults at mid-ocean ridges. Science (80-.). 329, 1047–1050.

Gerya, T. V, Yuen, D.A., 2007. Robust characteristics method for modelling multiphase visco-elasto-plastic thermo-mechanical problems. Phys. Earth Planet. Inter. 163, 83–105. doi:10.1016/j.pepi.2007.04.015

Hassan, R., Flament, N., Gurnis, M., Bower, D.J., Müller, M., 2015. Geochemistry, Geophysics, Geosystems. Geochemistry Geophys. Geosystems 18, 1541–1576. doi:10.1002/2014GC005684.Key

Heine, C., Zoethout, J., Müller, R.D., 2013. Kinematics of the South Atlantic rift. Solid Earth 4, 215–253. doi:10.5194/se-4-215-2013

Heit, B., Sodoudi, F., Yuan, X., Bianchi, M., Kind, R., 2007. An S receiver function analysis of the lithospheric structure in South America. Geophys. Res. Lett. 34, 1–5. doi:10.1029/2007GL030317

Hirsch, K.K., Scheck-Wenderoth, M., Wees, J.-D. Van, Kuhlmann, G., Paton, D.A., 2010. Tectonic

568 subsidence history and thermal evolution of the Orange Basin. Mar. Pet. Geol. 27, 565–584.
569 doi:10.1016/j.marpetgeo.2009.06.009
570 Husson, L., Conrad, C.P., Faccenna, C., 2012. Plate motions, Andean orogeny, and volcanism above the
571 South Atlantic convection cell. Earth Planet. Sci. Lett. 317–318, 126–135.
572 Koptev, A., Burov, E., Calais, E., Leroy, S., Gerya, T., Guillou-Frottier, L., Cloetingh, S., 2016.
573 Contrasted continental rifting via plume-craton interaction: Applications to Central East African Rift.
574 Geosci. Front. 7, 221–236. doi:10.1016/j.gsf.2015.11.002
575 Koptev, A., Calais, E., Burov, E., Leroy, S., Gerya, T., 2015. Dual continental rift systems generated by
576 plume – lithosphere interaction. Nat. Geosci. 8, 388–392. doi:10.1038/NGEO2401
577 Le Pourhiet, L., Burov, E., Moretti, I., 2004. Rifting through a stack of inhomogeneous thrusts (the
578 dipping pie concept). Tectonics 23, 1–14. doi:10.1029/2003TC001584
579 Lithgow-Bertelloni, C., Silver, P., 1998. Dynamic topography, plate driving forces and the African
580 superswell. Nature 395, 345–348. doi:10.1038/26212
581 Maystrenko, Y.P., Scheck-Wenderoth, M., Hartwig, A., Anka, Z., Watts, A.B., Hirsch, K.K., Fishwick, S.,
582 2013. Structural features of the Southwest African continental margin according to results of
583 lithosphere-scale 3D gravity and thermal modelling. Tectonophysics 604, 104–121.
584 doi:10.1016/j.tecto.2013.04.014
585 Mohriak, W.U., Mello, M.R., Vieira, I.S., Bassetto, M., Koutsoukos, E.A.M., 2000. Crustal architecture,
586 sedimentation, and petroleum systems in the Sergipe-Alagoas Basin, Northeastern Brazil. AAPG
587 Spec. Vol. 273–300.
588 Moulin, M., Aslanian, D., Unternehr, P., 2010. A new starting point for the South and Equatorial Atlantic
589 Ocean. Earth-Science Rev. 98, 1–37. doi:10.1016/j.earscirev.2009.08.001
590 Müller, R.D., Sdrolias, M., Gaina, C., Roest, W.R., 2008. Age, spreading rates, and spreading asymmetry
591 of the world's ocean crust. Geochemistry, Geophys. Geosystems 9, 1–19.
592 doi:10.1029/2007GC001743
593 Nyblade, A.A., Robinson, S.W., 1994. The African Superswell. Geophys. Res. Lett. 21, 765–768.

Poliakov, A.N.B., Podladchikov, Y., Talbot, C., 1993. Initiation of salt diapirs with frictional overburdens: numerical experiments. Tectonophysics 228, 199–210. doi:10.1016/0040-1951(93)90341-G

Ranalli, G., 1995. Rheology of the Earth, 2nd edition. Chapmann and Hall, 413 pp.

Ribe, N.M., Christensen, U.R., 1994. Three-dimensional modeling of plume-lithosphere interaction. J. Geophys. Res. 99, 669–682.

Sandwell, D.T., Smith, W.H.F., 2009. Global marine gravity from retracked Geosat and ERS-1 altimetry: Ridge segmentation versus spreading rate. J. Geophys. Res. Solid Earth 114, 1–18. doi:10.1029/2008JB006008

Schnabel, M., Franke, D., Engels, M., Hinz, K., Neben, S., Damm, V., Grassmann, S., Pelliza, H., Dos Santos, P.R., 2008. The structure of the lower crust at the Argentine continental margin, South Atlantic at 44°S. Tectonophysics 454, 14–22. doi:10.1016/j.tecto.2008.01.019

Sleep, N.H., 2006. Mantle plumes from top to bottom. Earth-Science Rev. 77, 231–271. doi:10.1016/j.earscirev.2006.03.007

Torsvik, T.H., Rousse, S., Labails, C., Smethurst, M.A., 2009. A new scheme for the opening of the South Atlantic Ocean and the dissection of an Aptian salt basin. Geophys. J. Int. 177, 1315–1333. doi:10.1111/j.1365-246X.2009.04137.x

Torsvik, T.H., Smethurst, M.A., Burke, K., Steinberger, B., 2006. Large igneous provinces generated from the margins of the large low-velocity provinces in the deep mantle. Geophys. J. Int. 167, 1447–1460. doi:10.1111/j.1365-246X.2006.03158.x

Tsenn, M.C., Carter, N.L., 1987. Upper limits of power law creep of rocks. Tectonophysics 136, 1–26. doi:10.1016/0040-1951(87)90332-5

Turcotte, D.L., Schubert, G., 2002. Geodynamics. Cambridge Univ. Press, Cambridge, UK.

Van Der Meijde, M., Julià, J., Assumpção, M., 2013. Gravity derived Moho for South America. Tectonophysics 609, 456–467. doi:10.1016/j.tecto.2013.03.023

Yamato, P., Burov, E., Agard, P., Le Pourhiet, L., Jolivet, L., 2008. HP-UHP exhumation during slow continental subduction: Self-consistent thermodynamically and thermomechanically coupled model

620 with application to the Western Alps. Earth Planet. Sci. Lett. 271, 63–74.
621 doi:10.1016/j.epsl.2008.03.049
622 Ziegler, P.A., Cloetingh, S., 2004. Dynamic processes controlling evolution of rifted basins. Earth-Science
623 Rev. 64, 1–50. doi:10.1016/S0012-8252(03)00041-2
624

Figure captions

Figure 1. Map of the South Atlantic domain with the location of large fracture zones, high velocity bodies (red ellipsoids), onshore graben structures (black dashed lines), the outline of the African Super Plume (dashed green line, after Davaille et al. (2015)) and the African superswell (dashed red line, after Nyblade and Robinson, 1994). Also shown are the extent of the Seaward Dipping Reflectors (SDR's, blue after Moulin et al., 2010 and green after Torsvik et al., 2009) and the Aptian salt (yellow, after Torsvik et al., 2009) deposits. The orange line gives the location of the Gondwana Fold-and-Thrust-Belt. Pink solid lines mark locations of the lithosphere-scale cross-sections (South America: A-A'; South Africa: B-B', Fig. 2). Hotspots (red stars): Tr = Trinidad hotspot; StH = Saint Helena hotspot; Bv = Bouvet (Meteor) hotspot; Deep-rooted mantle plume (yellow star): TdC = Tristan deep-rooted hotspot.

Figure 2. Lithosphere scale cross-sections of present-day South Atlantic margins. The Moho depth varies from 10 to 30 km on the South American side from ocean to continent (Schnabel et al., 2008). On the African side the depth varies from less than 10 km to over 40 km, ocean to continent (Maystrenko et al., 2013). The lithosphere-asthenosphere boundary (LAB) varies from 50 km to 120 km, ocean to continent for Colorado basin on the Argentinean margin (Heit et al., 2007). The Orange Basin on the South African margin has a LAB depth ranging between 80 km and 200 km from ocean to continent (Fishwick, 2010). The location of anomalous bodies is depicted (in green) for the Colorado Basin (Schnabel et al., 2008) and the Orange Basin (Maystrenko et al., 2013). The gravity profile has been extracted from the global marine gravity map of Sandwell and Smith v18.1 (Sandwell and Smith, 2009).

Figure 3. Six tested numerical setups. a) Setup 1a: 4-layered weak rheology, crust 40 km thick, lithosphere 200 km thick. b) Setup 1b: strong 4-layered rheology, crust 40 km thick, lithosphere 200 km thick. c) Setup 2a: combined rheological profiles (weak on the left side, strong on the right side), crust 40 km thick, and

lithosphere 200 km (equal for both rheologies). d) Setup 2b: combined rheological strength envelopes, (weak on the left side, strong on the right side), crust 30 km thick on the right side and 40 km thick on the left side, lithosphere 180 km thick on the left side and 200 km thick on the right side, no complex contact geometries. e) Setup 3a: combined rheological strength envelopes, (weak on the left side, strong on the right side), crust 30 km thick on the right side and 40 km thick on the left side; lithosphere 180 km thick on the left side and 200 km thick on the right side. The contact between the two different crustal thicknesses is a low-angle geometry, dipping towards the right. f). Setup 3b: combined rheological strength envelopes, (weak on the left side, strong on the right side), crust 30 km on the right side and 40 km thick on the left side, lithosphere 180 km thick on the left side and 200 km thick on the right side. The contact between the two different crustal thicknesses is a low-angle geometry dipping towards the left.

Figure 4. Models with different rheology and plume location showing the most representative examples of the three modes of continental break-up. a) "Centred": Experiment 6, Setup 1, with a strong rheology and the anomaly located at 1200 km (200 km offset from the centre towards the right). At 2.1 Myr the first topographic response occurs. The break-up axis develops directly above the initial mantle plume position and mantle material reaches the surface. b) "Shifted": Experiment 12, Setup 2, with a laterally varying rheology and the anomaly positioned in the centre at 1000 km. At 2.1 Myr the first topographic variation shows with a larger extend than the "centred" break-up model. The break-up axis develops offset from the original mantle plume location and mantle material migrates towards the spreading centre, reaching the surface. c) "Distant": Experiment 23, Setup 3, has a laterally varying rheology and the anomaly is positioned in the centre at 1000 km. At 2.1 Myr minor topographic variation. The break-up axis develops far offset from the original mantle plume location and the mantle plume remains glued to the base of the lithosphere. The initial topographic variations remain visible after break-up.

Figure 5. Examples of models with different setup, plume location rheological structure showing the different modes of break-up; a-c) "centred" examples, d-f) "shifted" examples, g-i) "distant" examples. In

red the initial location of the mantle anomaly is drawn. The graphs below show the normalised, statistical likelihood of a mode ("centred", "shifted" or "distant") for a given setups.

Figure 6. Evolution of 3D model a) rapid plume uplift leading to formation of linear extension-perpendicular rift at the crustal level; b-c) development of wide rift basin with localized crustal high strain along bounding normal faults; gradual cooling and solidification of plume head material; d) widely distributed rift above completely crystallized plume head ponding lithosphere-asthenosphere boundary; e) rapid transition from deformation localized in normal faults bounding wide rift valley to localized strain within narrow zones associated with localized plume ascent; f) breakup of the continental lithosphere along spreading zone considerably shifted from centre of the mantle plume. Bulk of plume material is shown in pale orange. Green to red colours indicate strain rate at the level of 10 km (i.e. within upper crust). Component distribution is shown for vertical cross-sections trough central part of the model domain.

Figure 7. Detailed display of experiment 12. Setup 2 is the base for this experiment with a laterally varying rheology. The anomaly is positioned in the centre of the model at 1000 km. At 2.1 Myr the first topographic variation shows with a larger extend than the "centred" break-up model. Strain rate localizes slightly shifted from the plume impingement point at 3.1 Myr. Strain localizes, topography variations grow and crustal break-up occurs at 8.1 Myr. Mantle material slowly migrates towards the spreading centre reaching the surface until the material that remains below the lithosphere reaches thermal equilibrium around 22 Myr.

Figure 8. Schematic representation of the three modes of break-up. a) The very early phase of rifting (0 – 5 Myr) is very similar for all three modes after which they develop into b) "Centred"; c) "shifted" and d) "distant". An example of a simplified interpretation of the Uruguayan margin (after Clerc et al., 2015) is used to demonstrate the resemblance of the "shifted" mode of break-up, like experiment 12, with the South Atlantic domain. e) Map showing the outline of the plate configuration at the moment of break-up

between Africa and South America on the lower mantle low velocity zone (South African Super Plume) (from Davaille et al., 2005). The Parana-Etendeka flood basalts are depicted in green (after Torsvik et al., 2009). The orange dots refer to the three possible principal locations of initial thermal anomaly at the upper/lower mantle boundary corresponding to the Tristan plume

Table caption

Table 1. Summary of the thermal and mechanical parameters used for this study. 1) Turcotte and Schubert (2002), 2) Ranalli (1995); 3) d'Acremont et al. (2003) and references therein; 4) Tsenn and Carter (1987); 5) Burov and Poliakov (2001).

Table 2. Controlling parameters and principal results of the experiments.

Equatorial Segment
Central Segment
South Segment
Falkland Segment
Romanche Fracture Zone
Florianopolis Fracture Zone
Agulhas-Falkland Fracture Zone
Anambra Basin
Benua trough
Cameroon Basin
Niger Delta Basin
Rio Muni Basin
Gabon Basin
Gabon graben
Lower Congo Basin
Congo Basin
Kwanza Basin
Namibe Basin
Etendeka FB
Walvis Basin
Walvis Ridge
Luderitz Basin
Orange Basin
Cape Graben
Outarniqua Basin
Potiguar Basin
Potiguar
Pernambuco Basin
Sergipe Alagoas Basin
Reconcavo Basin
Tucano-Reconcavo graben
Camamu-Atmada Basin
Jequitinhonha Basin
Espirito Santo Basin
Campos Basin
Santos Basin
Pelotas Basin
Rio Grande Rise
StH
Tr
TdC
Bv
Andes
Puna plateau
Parana FB
Abimael ridge
Cumuruxatiba Basin
Canellos Graben
Rio Salada Graben
Colorado Graben
Salado Basin
Colorado Basin
Valdez Basin
Rawson Basin
San Jorge graben
San Jorge Basin
San Julian Basin
North Falkland Basin
Magallenas graben
South Falkland Basin
Malvinas Basin
Magallanes Basin
A
A′
B
B′
Gravity anomaly: mgals
21
11
2
-6
-16
N
Legend
Hotspot
Rooted mantle plume
Aptian salt depositions
Seaward dipping reflectors (SDR)
Outline South Africa superswell
Outline South African plume
Lithosphere-scale transect
Gondwana fold-and-thrustbelt
lower crustal gravity/velocity anomaly
onshore graben
Scale 1:1.000.000
0 km 500 1000
10°N
5°N
0°N
5°S
10°S
15°S
20°S
25°S
30°S
35°S
40°S
45°S
50°S
55°S
80°W
70°W
60°W
50°W
40°W
30°W
20°W
10°W
W0°E
10°E
20°E
30°E
40°E

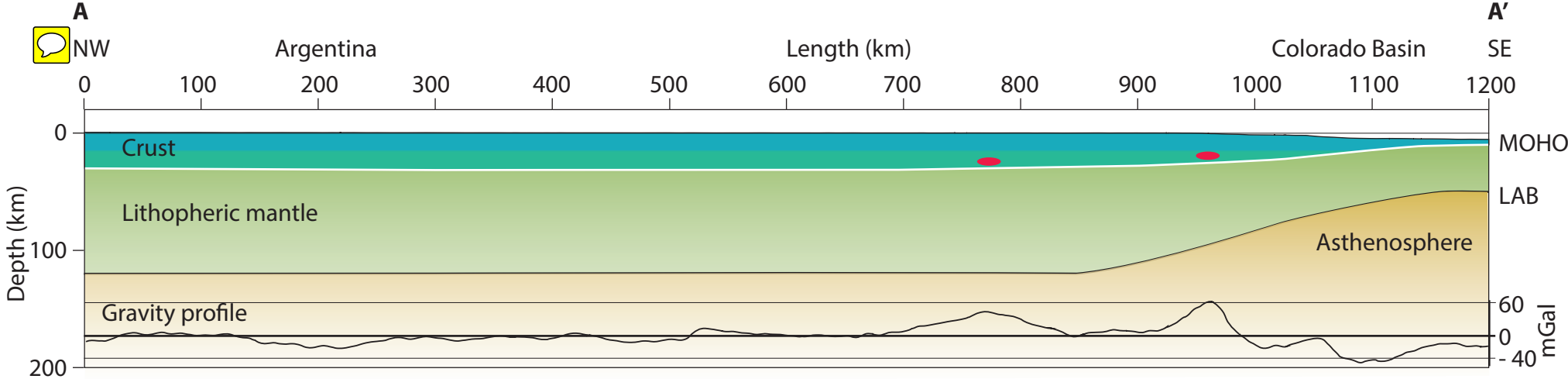

a. South America

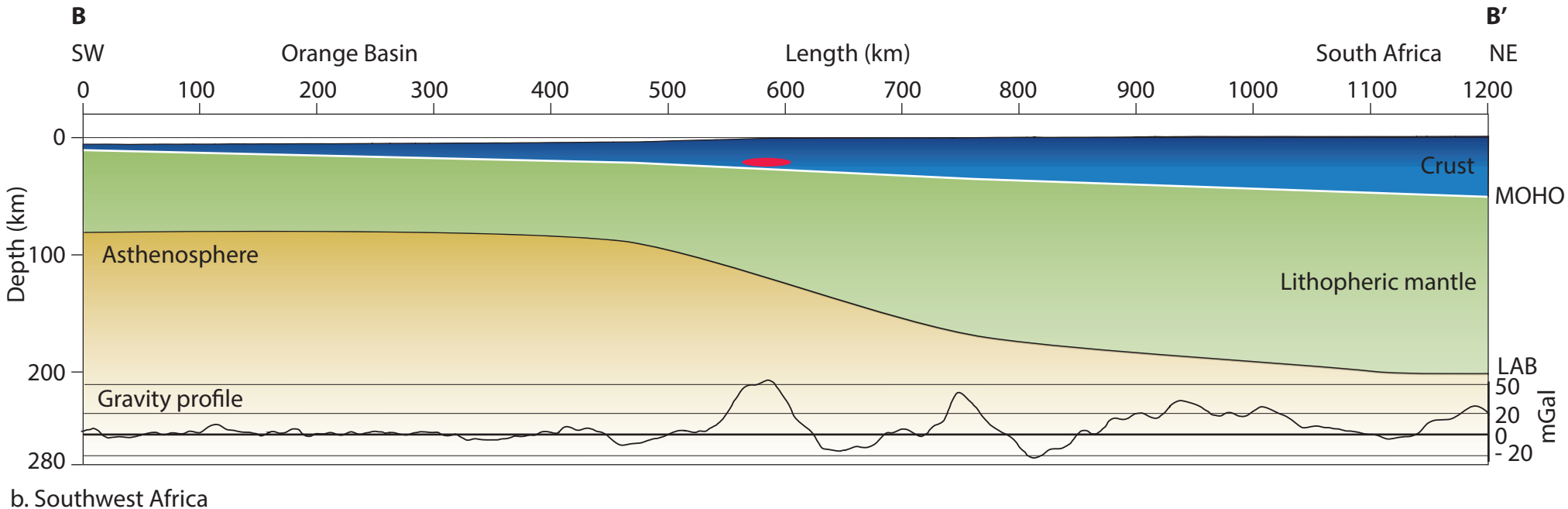

b. Southwest Africa

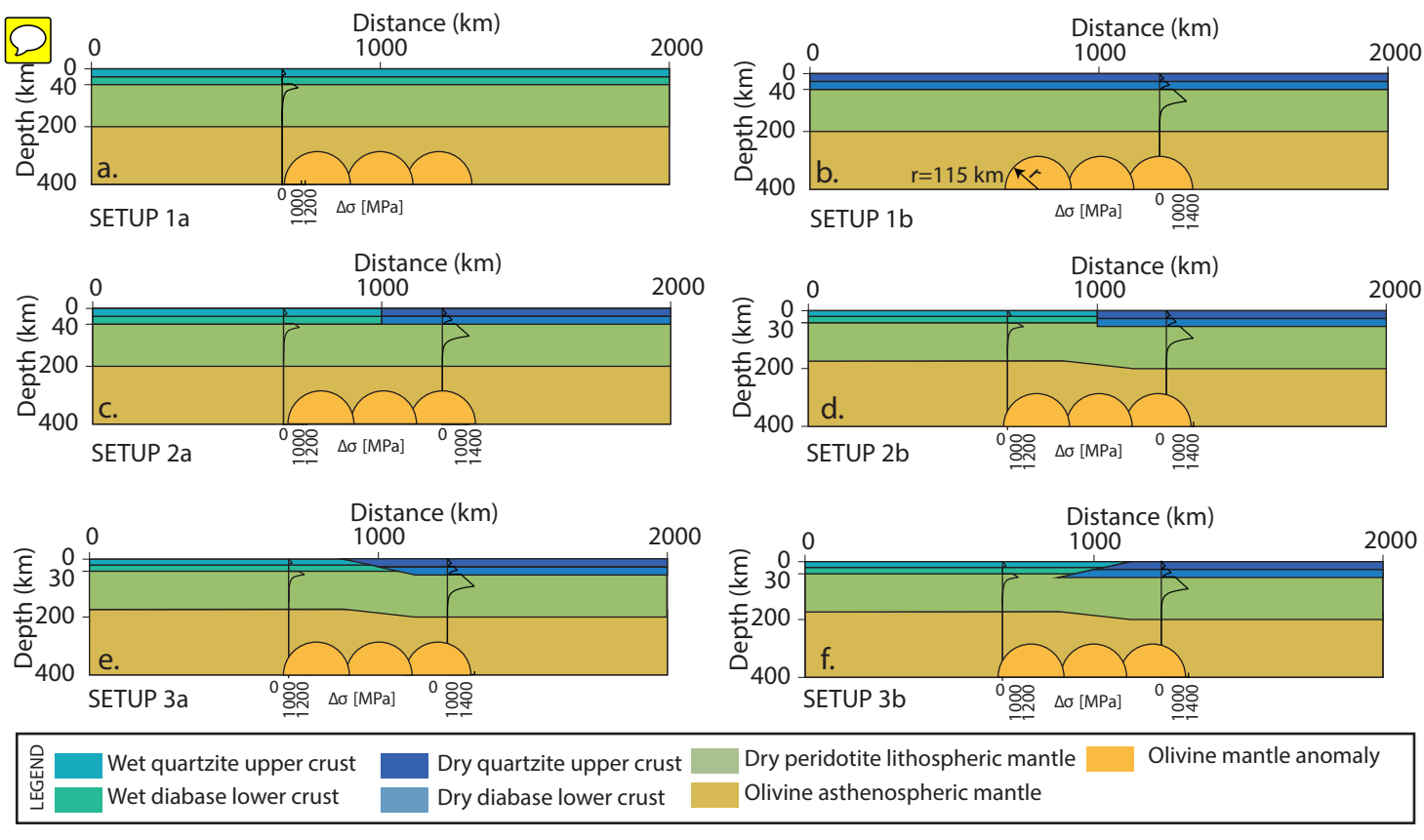
Distance (km)
0
1000
2000
Depth (km)
0
40
200
400
a.
SETUP 1a
Δσ [MPa]
0
1000
1200
b.
r=115 km
SETUP 1b
1400
c.
SETUP 2a
d.
SETUP 2b
30
e.
SETUP 3a
f.
SETUP 3b
LEGEND
Wet quartzite upper crust
Wet diabase lower crust
Dry quartzite upper crust
Dry diabase lower crust
Dry peridotite lithospheric mantle
Olivine asthenospheric mantle
Olivine mantle anomaly

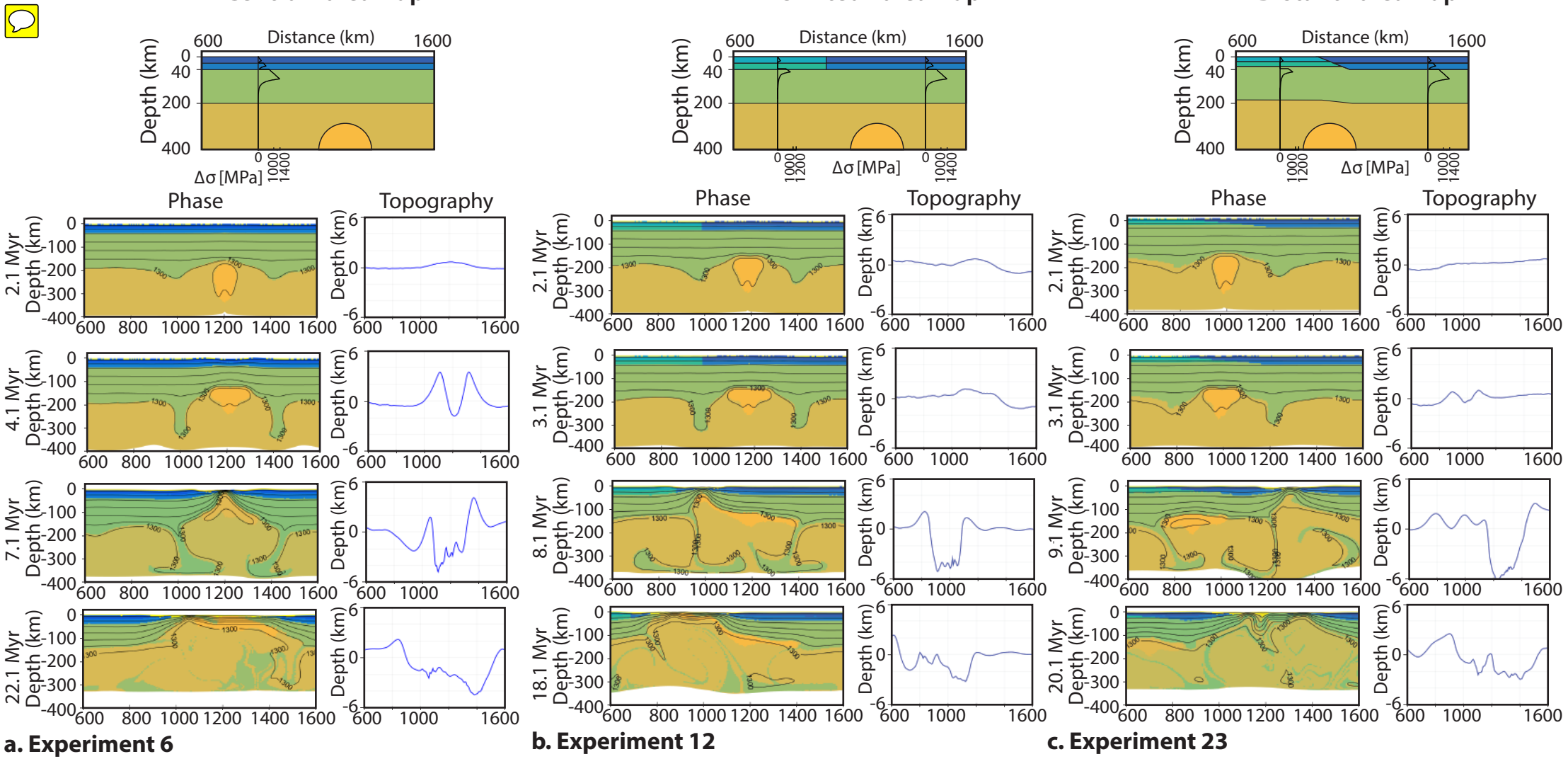
"Central" break-up
"Shifted" break-up
"Distant" break-up
Distance (km)
Depth (km)
Δσ [MPa]
Phase
Topography
2.1 Myr
4.1 Myr
7.1 Myr
22.1 Myr
3.1 Myr
8.1 Myr
18.1 Myr
9.1 Myr
20.1 Myr
a. Experiment 6
b. Experiment 12
c. Experiment 23

"Central" break-up

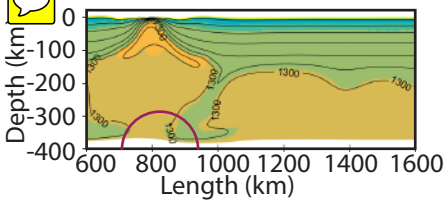

a. Experiment 1 @ 7 Myr

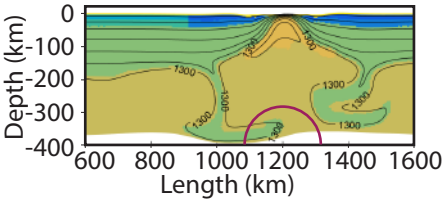

b. Experiment 9 @ 8 Myr

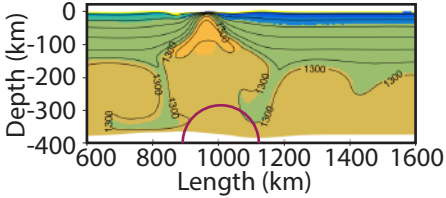

c. Experiment 17 @ 7 Myr

"Shifted" break-up

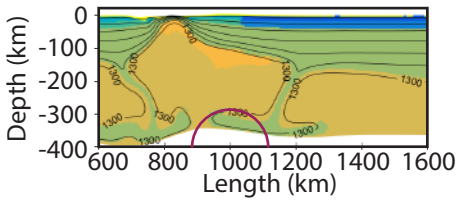

d. Experiment 11 @ 9 Myr

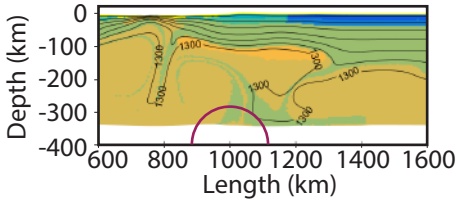

e. Experiment 8 @ 17 Myr

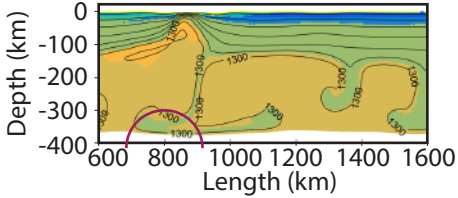

f. Experiment 34 @ 9 Myr

"Distant" break-up

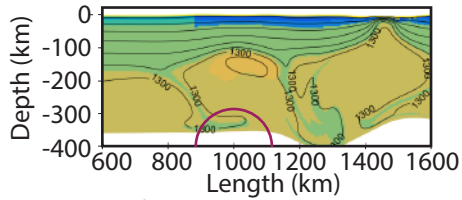

g. Experiment 14 @ 11 Myr

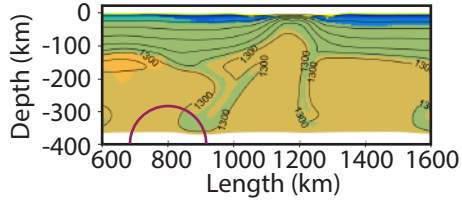

h. Experiment 22 @ 10 Myr

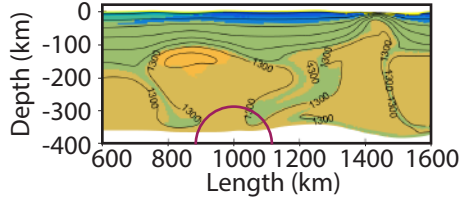

i. Experiment 35 @ 10 Myr

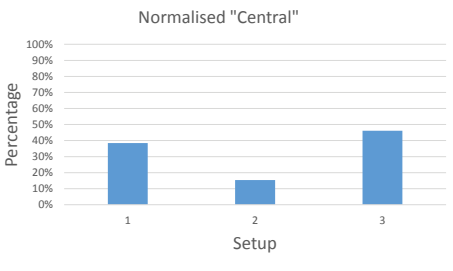

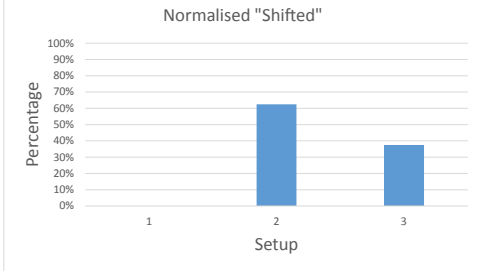

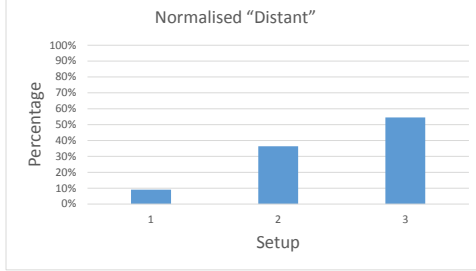

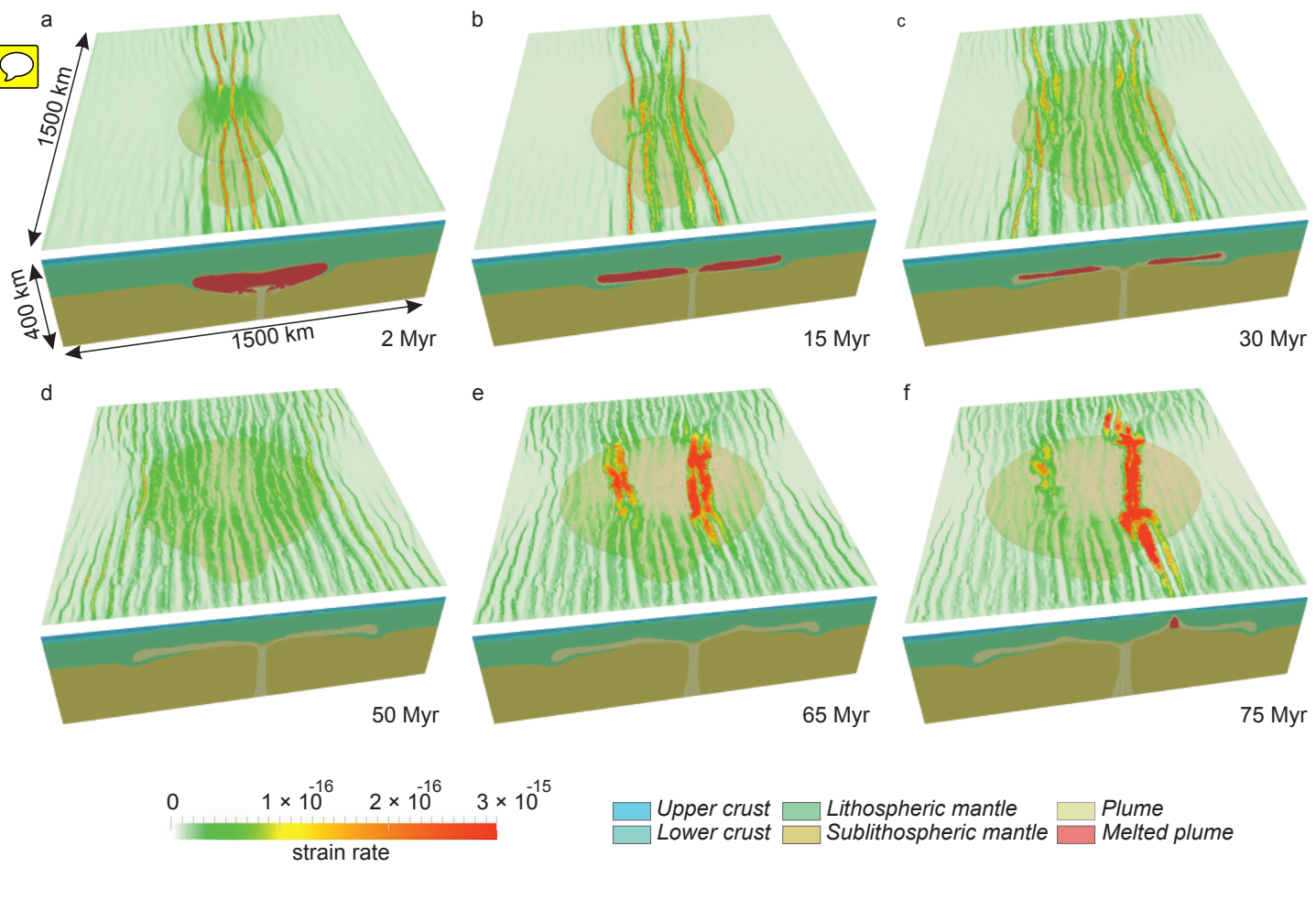
a
1500 km
400 km
1500 km
2 Myr
b
15 Myr
c
30 Myr
d
50 Myr
e
65 Myr
f
75 Myr
0
1 × 10-16
2 × 10-16
3 × 10-15
strain rate
Upper crust
Lower crust
Lithospheric mantle
Sublithospheric mantle
Plume
Melted plume

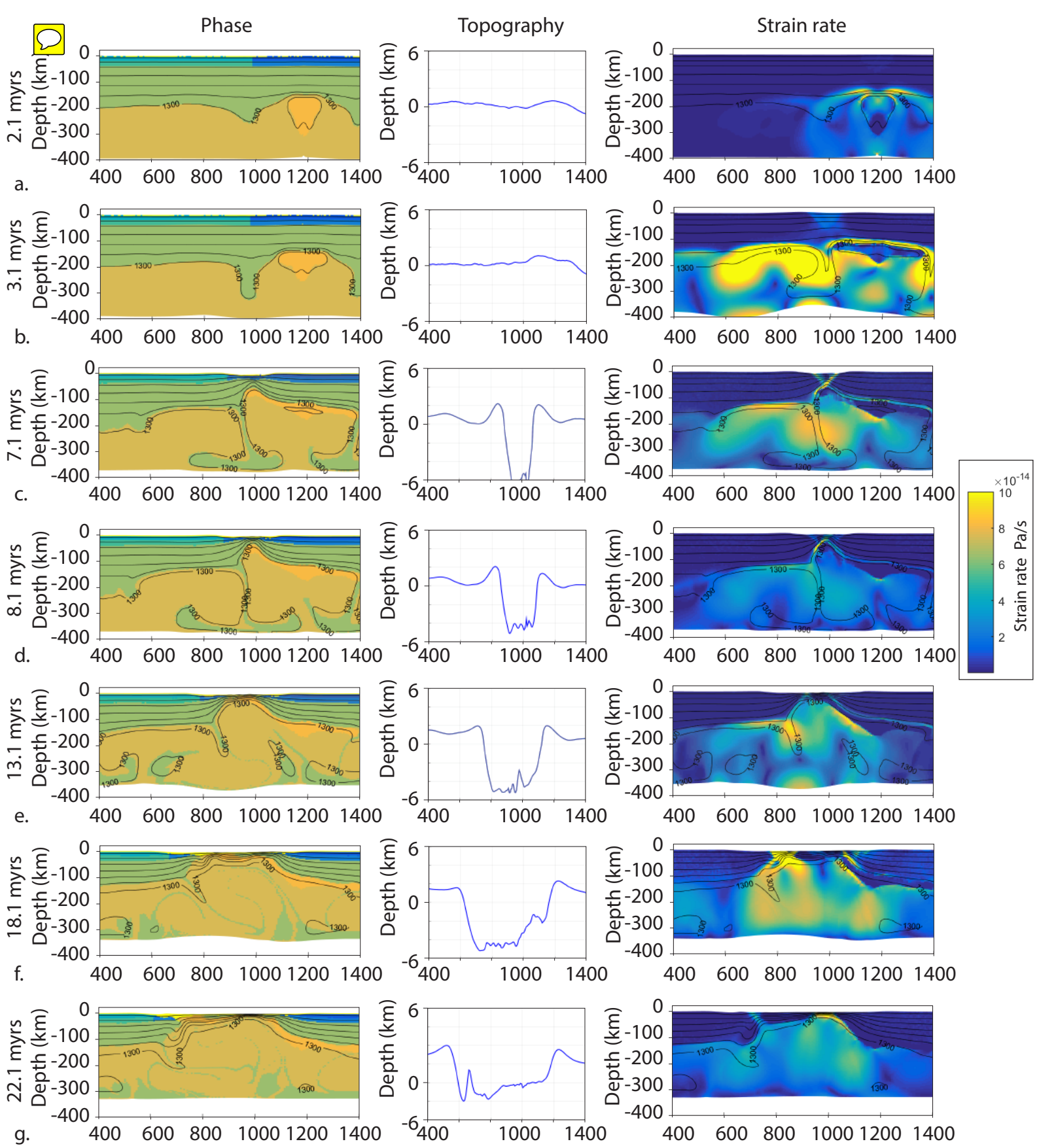
Phase
Topography
Strain rate
2.1 myrs
3.1 myrs
7.1 myrs
8.1 myrs
13.1 myrs
18.1 myrs
22.1 myrs
Depth (km)
0
-100
-200
-300
-400
6
0
-6
400
600
800
1000
1200
1400
1300
a.
b.
c.
d.
e.
f.
g.
×10-14
10
8
6
4
2
Strain rate Pa/s

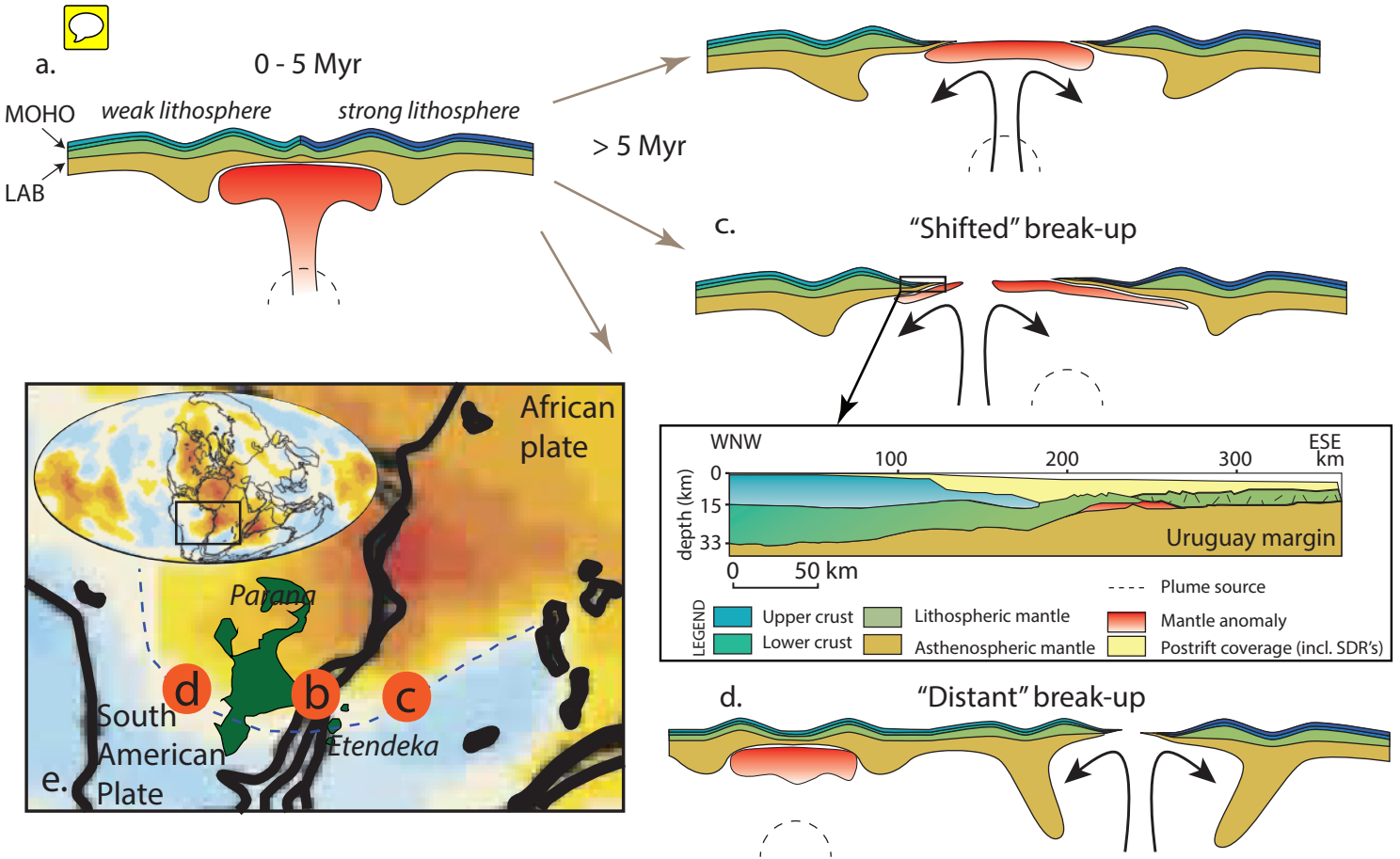
a.
0 - 5 Myr
MOHO
LAB
weak lithosphere
strong lithosphere
> 5 Myr
b.
"Central" break-up
c.
"Shifted" break-up
WNW
ESE
100
200
300
km
0
15
33
depth (km)
Uruguay margin
0
50 km
Plume source
LEGEND
Upper crust
Lower crust
Lithospheric mantle
Asthenospheric mantle
Mantle anomaly
Postrift coverage (incl. SDR's)
d.
"Distant" break-up
African plate
Paraná
d
b
c
South American Plate
Etendeka
e.

712 **Tables**

713 **Table 1**

Thermal parameters	Thermal property	Value	Unit	Ref.
	Surface temperature	10	°C	1
	Temperature at the base of the thermal lithosphere	1330	°C	
	Temperature at the base of the upper mantle	1400	°C	
	Temperature mantle anomaly	1700	°C	
	Thermal conductivity crust	2.5	W/m °C	
	Thermal conductivity mantle	3.5	W/m °C	
	Radiogenic heat production at the surface	1.5E-9	W/kg	
	Radius radiogenic heat	10	km	
	Thermo-tectonic age of the lithosphere	500	myrs	
	Surface heat flow	40	mW/m^2	
	Mantle heat flow	15	mW/m^2	
Mechanical parameters	**Mechanical property**			
Strong upper crust	density	2600	kg/m^3	2
Dry quarts	Viscosity parameter N	3		
	Viscosity parameter A	6.8e-6	MPa^-n/s^-1	
	Viscosity parameter E	1.56e5	J/mol	
Strong lower crust	density	2850	kg/m^3	3
Strong diabase	Viscosity parameter N	3.05		
	Viscosity parameter A	6.3e-2	Mpa^-n/s^-1	
	Viscosity parameter E	2.76e5	J/mol	
Weak upper crust	density	2500	kg/m^3	2
Wet quartz	Viscosity parameter N	2.3		
	Viscosity parameter A	3.2e-4	Mpa^-n/s^-1	
	Viscosity parameter E	1.54e5	J/mol	
Weak lower crust	density	2750	kg/m^3	4
Weak diabase	Viscosity parameter N	4.7		
	Viscosity parameter A	1.9e2	Mpa^-n/s^-1	
	Viscosity parameter E	4.85e5	J/mol	
Lithospheric mantle	density	3330	kg/m^3	2
Peridotite	Viscosity parameter N	3.5		
	Viscosity parameter A	2.5e4	Mpa^-n/s^-1	
	Viscosity parameter E	5.32e5	J/mol	
Asthenosphere	density	3310	kg/m^3	3
Olivine	Viscosity parameter N	3.2		
	Viscosity parameter A	7.0e3	Mpa^-n/s^-1	
	Viscosity parameter E	5.1e5	J/mol	
Plume	density	3250	kg/m^3	3
Olivine	Viscosity parameter N	3.5		
	Viscosity parameter A	5.e14	Mpa^-n/s^-1	
	Viscosity parameter E	5.2e5	J/mol	
	Friction angle	30	°	
	Lamé elastic constant λ=G	25	GPa	
	Cohesion	20	MPa	
	Erosion coefficient (a)	500	m^2/yr	5

714

715 **Table 2**

	Controlling parameters Boundary conditions		Mantle plume properties			Setup	Results			
	Extension rate (left)	**Extension rate (right)**	**Plume location**	**Density (kg/m^3)**	**Diameter (km)**	**Initial geometry**	**Break-up point**	**Above center anomaly?**	**Break-up mechanism**	**Figure**
1	12.5 mm/yr	12.5 mm/yr	800 km	3250	230	Setup 1a	800 km	yes	Central	5a
2	12.5 mm/yr	12.5 mm/yr	1000 km	3250	230	Setup 1a	1500 km	no	Distant	
3	12.5 mm/yr	12.5 mm/yr	1200 km	3250	230	Setup 1a	1200 km	yes	Central	
4	12.5 mm/yr	12.5 mm/yr	800 km	3250	230	Setup 1b	800 km	yes	Central	
5	12.5 mm/yr	12.5 mm/yr	1000 km	3250	230	Setup 1b	1000 km	yes	Central	
6	12.5 mm/yr	12.5 mm/yr	1200 km	3250	230	Setup 1b	1200 km	yes	Central	4a
7	12.5 mm/yr	12.5 mm/yr	800 km	3250	230	Setup 2a	850 km	no	Shifted	
8	12.5 mm/yr	12.5 mm/yr	1000 km	3250	230	Setup 2a	800 km	no	Shifted	5e
9	12.5 mm/yr	12.5 mm/yr	1200 km	3250	230	Setup 2a	1200 km	yes	Central	5b
10	20 mm/yr	5 mm/yr	800 km	3250	230	Setup 2a	750 km	no	Shifted	
11	20 mm/yr	5 mm/yr	1000 km	3250	230	Setup 2a	800 km	no	Shifted	5d
12	20 mm/yr	5 mm/yr	1200 km	3250	230	Setup 2a	1000 km	no	Shifted	4b/7
13	12.5 mm/yr	12.5 mm/yr	800 km	3250	230	Setup 2b	1600 km	no	Distant	
14	12.5 mm/yr	12.5 mm/yr	1000 km	3250	230	Setup 2b	1450 km	no	Distant	5g
15	12.5 mm/yr	12.5 mm/yr	1200 km	3250	230	Setup 2b	xxx	xxx	no break-up	
16	20 mm/yr	5 mm/yr	800 km	3250	230	Setup 2b	1200 km	no	Distant	
17	20 mm/yr	5 mm/yr	1000 km	3250	230	Setup 2b	1000 km	yes	Central	5c
18	20 mm/yr	5 mm/yr	1200 km	3250	230	Setup 2b	1700 km	no	Distant	
19	12.5 mm/yr	12.5 mm/yr	800 km	3250	230	Setup 3a	1200 km	no	Distant	
20	12.5 mm/yr	12.5 mm/yr	1000 km	3250	230	Setup 3a	1000 km	yes	Central	
21	12.5 mm/yr	12.5 mm/yr	1200 km	3250	230	Setup 3a	1200 km	yes	Central	
22	20 mm/yr	5 mm/yr	800 km	3250	230	Setup 3a	1200 km	no	Distant	5h
23	20 mm/yr	5 mm/yr	1000 km	3250	230	Setup 3a	1300 km	no	Distant	4c
24	20 mm/yr	5 mm/yr	1200 km	3250	230	Setup 3a	1250 km	yes	Shifted	
31	12.5 mm/yr	12.5 mm/yr	800 km	3250	230	Setup 3b	800 km	yes	Central	
32	12.5 mm/yr	12.5 mm/yr	1000 km	3250	230	Setup 3b	1000 km	yes	Central	
33	12.5 mm/yr	12.5 mm/yr	1200 km	3250	230	Setup 3b	1200 km	yes	Central	
34	20 mm/yr	5 mm/yr	800 km	3250	230	Setup 3b	850 km	no	Shifted	5f
35	20 mm/yr	5 mm/yr	1000 km	3250	230	Setup 3b	1400 km	no	Distant	5i
36	20 mm/yr	5 mm/yr	1200 km	3250	230	Setup 3b	1700 km	no	Distant	